2015

Yolk-shell silicon-mesoporous carbon anode with compact solid electrolyte interphase film for superior lithium-ion batteries

Jianping Yang
University of Wollongong

Yunxiao Wang
University of Wollongong, yunxiao@uow.edu.au

Shulei Chou
University of Wollongong, shulei@uow.edu.au

Renyuan Zhang
Fudan University

Yanfei Xu
University of Wollongong, yx867@uowmail.edu.au

See next page for additional authors

Yolk-shell silicon-mesoporous carbon anode with compact solid electrolyte interphase film for superior lithium-ion batteries

Abstract

Silicon as an electrode suffers from short cycling life, as well as unsatisfactory rate-capability caused by the large volume expansion (~400%) and the consequent structural degradation during lithiation/delithiation processes. Here, we have engineered unique void-containing mesoporous carbon-encapsulated commercial silicon nanoparticles (NPs) in yolk-shell structures. In this design, the silicon NPs yolk are wrapped into open and accessible mesoporous carbon shells, the void space between yolk and shell provides enough room for Si expansion, meanwhile, the porosity of carbon shell enables fast transport of Li+ ions between electrolyte and silicon. Our ex-situ characterization clearly reveals for the first time that a favorable homogeneous and compact solid electrolyte interphase (SEI) film is formed along the mesoporous carbon shells. As a result, such yolk-shell Si@mesoporous-carbon nanoparticles with a large void exhibits long cycling stability (78.6% capacity retention as long as 400 cycles), and superior rate-capability (62.3% capacity retention at a very high current density of 8.4Ag-1).

Keywords

interphase, film, superior, lithium, ion, batteries, electrolyte, compact, solid, anode, carbon, mesoporous, yolk, silicon, shell

Disciplines

Engineering | Physical Sciences and Mathematics

Authors

Jianping Yang, Yunxiao Wang, Shulei Chou, Renyuan Zhang, Yanfei Xu, Jianwei Fan, Weixian Zhang, Hua-Kun Liu, Dongyuan Zhao, and S X. Dou

Yolk-shell silicon-mesoporous carbon anode with compact solid electrolyte interphase film for superior lithium-ion batteries

Jianping Yang,‡ [a,b,c] Yunxiao Wang,‡[b,c] Shulei Chou,[b] Renyuan Zhang,[c] Yanfei Xu,[b] Jianwei Fan,[a] Wei-xian Zhang,*[a] Hua Kun Liu,[b] Dongyuan Zhao,*[c] and Shi Xue Dou*[b]

[a] College of Environmental Science and Engineering, State Key Laboratory of Pollution Control and Resources Reuse, Tongji University, Shanghai 200092, P. R. China

[b] Institute for Superconducting & Electronic Materials, Australian Institute of Innovative Materials, University of Wollongong, Innovation Campus, Squires Way, North Wollongong, NSW 2500, Australia

[c] Department of Chemistry, Laboratory of Advanced Materials, Fudan University, Shanghai 200433, P. R. China

[‡] These authors contributed equally to this work.

E-mail: zhangwx@tongji.edu.cn (W. Zhang);

dyzhao@fudan.edu.cn (D. Zhao), Tel.: +86-21-5163-0205;

shi_dou@uow.edu.au (S. Dou)

Abstract: Silicon as an electrode suffers from short cycling life, as well as unsatisfactory rate-capability caused by the large volume expansion (~ 400 %) and the consequent structural degradation during lithiation/delithiation processes. Here, we have engineered unique void-containing mesoporous carbon-encapsulated commercial silicon nanoparticles (NPs) in yolk-shell structures. In this design, the silicon NPs yolk are wrapped into open and accessible mesoporous carbon shells, the void space between yolk and shell provides enough room for Si expansion, meanwhile, the porosity of carbon shell enables fast transport of Li^+ ions between electrolyte and silicon. Our *ex-situ* characterization clearly reveals for the first time that a favorable homogeneous and compact solid electrolyte interphase (SEI) film is formed along the mesoporous carbon shells. As a result, such yolk-shell Si@mesoporous-carbon nanoparticles with a large void exhibits long cycling stability (78.6 % capacity retention as long as 400 cycles), and superior rate-capability (62.3% capacity retention at a very high current density of 8.4 A g^{-1}).

Keywords: mesoporous carbon, yolk-shell, sol-gel, void space, lithium ion battery

1. Introduction

Developing rechargeable lithium ion batteries (LIBs) with a long cycling life, high energy density, and excellent rate-capability is of critical importance for electric vehicles and renewable energy storage [1-4]. The traditional graphite anode with its limited theoretical capacity of ~ 372 mA h g^{-1}, is unable to meet the high energy needs of such applications. Various anode materials and strategies have been explored and proposed for increasing the specific capacity of LIBs [5-7]. Due to its high theoretical capacity (Li$_{4.4}$Si = 4200 mA h g^{-1}) and low discharge potential (~ 0.5 V versus Li/Li^{+}), silicon has been considered as an attractive and promising candidate for LIBs [8]. The practical application of Si-based anodes, however, is still hindered by two critical problems: the relatively low electric conductivity and the huge volume expansion (~ 400 %) upon lithium insertion and extraction [9]. These often cause fracturing, pulverization, and loss of electrical contact, leading to rapid capacity fading and poor cycling performance [10].

It is a common and effective strategy to adopt nanoscale silicon materials with various morphologies, including nanoparticles [11, 12], nanowires [13], nanotubes [14, 15], and hollow spheres [16, 17]. Compared to bulk silicon, such nanostructured Si is able to accommodate elevated mechanical stress, resulting in prolonged cycling stability. Nanostructured silicon materials, however, still suffer from poor electric conduction [18]. Further optimization is achieved by incorporating nano-silicon materials with various conductive matrixes, such as graphene [19, 20], carbon nanotubes [21], and carbon [22, 23] to form core-shell and yolk-shell nanocomposites [24]. The most promising carbon coating strategy has been explored to promote the electrochemical performance [25-28]. The obvious advantage of carbon shells is intensive improving the overall electrical conductivity of the Si-based anodes. In addition, the introduction of such a carbon shell plays a key role in alleviating the agglomeration of nano-silicon particles [29, 30]. However, the well-established carbon coating methods are based on the chemical vapor deposition, hydrothermal of carbohydrates and polymerization of phenolic resin from sol-gel process, all of them unfortunately result in the compact carbon shells without open and connecting

mesopore channels for fast transport of Li^+ ions between the electrolyte and silicon. This could be the reason that Si NPs covered with carbon layer matrix as an anode present unsatisfactory rate-capability [18, 29, 31]. Furthermore, the crucial impact of SEI is usually be neglected and the formation of SEI is hard to control. Importantly, if a stable and compact SEI is constructed, the electrolyte molecules would not penetrate through SEI layer into the active material for further growth, thereby avoiding continual lithium loss and ensuring higher Coulombic efficiency.

Here, aiming at outstanding cycling stability and rate-capability, we report a novel large-void-containing Si@mesoporous carbon yolk-shell structure from commercial silicon NPs for LIB anodes. This unique design has multiple attractive advantages: (i) the special design of the void spaces (10 and 50 nm) between the silicon NPs and the mesoporous carbon shells highlights the superiority of the unique yolk-shell structure and allows us to optimize the cycling stability while maintaining a reasonable storage capacity; (ii) the open-ended mesoporous carbon shells with accessible channels are able to facilitate the fast diffusion of Li^+ ions, and guarantee the full immersion of active materials in the electrolyte, thus contributing to excellent rate capability; (iii) the mesoporous carbon shells are beneficial for the formation of a homogeneous and compact SEI-layer film on the external surface, retaining the internal void space for silicon yolk expansion and rendering superior capacity retention at a high current density. With this design, such elegant mesoporous carbon-encapsulated Si yolk-shell NPs address the challenges of rapid capacity decay and unsatisfied rate capability for Si-anodes, and deliver a high reversible capacity of ~ 1000 mA h g^{-1} with outstanding cyclability during 400 long-deep cycles, as well as superior rate-capability at a very high current density of 8.4 A g^{-1}.

2. Experimental section

Chemicals: All of the chemicals were analytical grade and used without further purification. Commercial silicon nanoparticles the size ranging from ~ 60 to 170 nm were obtained from Nanostructured and Amorphous Materials, Inc. 2-propanol, ammonia aqueous solution (28 wt %), tetraethyl orthosilicate (TEOS),

hexadecyltrimethylammonium bromide (CTAB), NH_4NO_3, NaOH, HCl, HF, phenol, and formalin solution (37 wt %) were purchased from Sinopharm Chemical Reagent Co., Ltd. Deionized water was used in all experiments.

Synthesis of Si@SiO₂ Core-Shell Nanoparticles: The commercial silicon nanoparticles the size ranging from ~ 60 to 170 nm were first coated with silica layers with different thicknesses according to the Stöber sol-gel method. In a typical synthesis of the SiO_2 coating with the thickness of ~ 50 nm, 0.15 g commercial Si nanoparticles were dispersed in a mixed solution containing deionized water (70 mL), ethanol (280 mL), and ammonia (5 mL, 28 wt %) under ultrasound for 20 min. Afterwards, 1.0 mL TEOS was added dropwise every 30 min (4.0 mL in total), and the reaction continued at 25 °C for 10 h under continuous mechanical stirring (220 rpm). The core-shell $Si@50SiO_2$ nanoparticles were obtained after centrifugation and washing with ethanol several times.

For the SiO_2 coating with the thickness of ~ 10 nm, 0.1 g commercial Si nanoparticles were added to 200 mL 2-propanol, and a homogeneous solution was formed by exposure to ultrasound for 30 min. 10 mL ammonia aqueous solution (28 wt %) and 18 mL H_2O were poured into the dispersion and stirred (600 rpm) at 40 °C for 30 min. Then, 0.1 mL TEOS was injected and reacted for 2 h. The $Si@10SiO_2$ nanoparticles were collected by centrifugation and washed with ethanol several times.

Synthesis of Si@SiO₂@mSiO₂ Core-Shell Nanoparticles: The mesoporous silica (mSiO₂) with thickness of ~ 15 nm was deposited on the surface of the Si@SiO₂ nanoparticles through a well-established surfactant-templating sol-gel route with CTAB as the template. Typically, 0.15 g $Si@50SiO_2$ nanoparticles and 0.225 g CTAB were added into a solution of deionized water (75 mL), ethanol (45 mL), and ammonia (0.825 mL, 28 wt %). The mixture became a homo-geneously dispersed solution after treatment with ultrasound and stirring, for 30 min each, and then 0.12 mL TEOS was injected. The reaction was allowed to proceed for 6 h at 25 °C under gentle stirring. The products were collected by centrifugation, washed with ethanol, and re-dispersed into 60 mL NH_4NO_3/ethanol (6 g/L) solution for removal of the CTAB surfactant. This extraction process proceeded at 60 °C for 10 h to yield

core-shell Si@50SiO$_2$@mSiO$_2$ nanoparticles. The core-shell Si@10SiO$_2$@mSiO$_2$ nanoparticles were synthesized by a method similar to the above process, but with 0.188 mL TEOS added as the silica source.

Preparation of Phenolic resin Precursors: Low-molecular-weight resol precursors were prepared as the carbon source. Briefly, 8 g phenol was melted at 45 °C and mixed with NaOH aqueous solution (1.36 g, 20 wt %). This was followed by the dropwise addition of formalin solution (14.2 g, 37 wt %) under magnetic stirring. Upon further reaction for 1 h at 70 °C, the solution was cooled to room temperature and adjusted to neutral pH (pH ≈ 7) with HCl (0.6 M). The water in the solution was removed by vacuum evaporation at 50 °C.

Synthesis of Si@mC Yolk-Shell Nanoparticles: The mesoporous carbon shell was fabricated *via* a nanocasting route by using phenolic resin as the carbon source. In a typical procedure, 0.2 g of Si@50SiO$_2$@mSiO$_2$ nanoparticles was dispersed in 5.0 mL ethanol, followed by the addition of 1.0 g of the above-prepared resol. The mixture was stirred at room temperature while open to air to evaporate the ethanol solvent. The dried powder was calcined at 900 °C for 3 h under a nitrogen atmosphere to obtain a carbon-covered composite (Si@50SiO$_2$@mSiO$_2$-C). Finally, the mesoporous SiO$_2$ hard template and the SiO$_2$ middle layer were removed to create the mesoporous carbon shell and the void space by etching with 1 wt % hydrofluoric acid solution. The etching process was conducted overnight at room temperature, followed by a washing with excess deionized water. The resultant yolk-shell Si@50mC nanoparticles were dried at 60 °C in vacuum for further characterization.

Characterization: The core-shell structures and diameters were further investigated by transmission electron microscopy (TEM, JEOL-2010) operated at an acceleration voltage of 200 kV. The samples were suspended in ethanol and dried on a holey carbon film on a Cu grid for TEM measurements. The morphologies of the samples were observed on a Hitachi S-4800 (Japan) field-emission scanning electron microscope (FESEM). The porosity was measured by nitrogen sorption isotherms at 77 K with a Micromeritics Tristar 3020 analyzer (USA). Before measurements, the samples were degassed in vacuum at 180 °C for at least 6 h. The

Brunauer-Emmett-Teller (BET) method was utilized to calculate the specific surface areas (S_{BET}), using adsorption data in a relative pressure (P/P_0) range from 0.04 to 0.2. The pore volume and pore size distributions were derived from the adsorption branches of isotherms by using the Barrett-Joyner-Halenda (BJH) model. The total pore volume, V_t, was estimated from the amount adsorbed at a relative pressure P/P_0 of 0.995. The ordering of materials was characterized by small-angle X-ray scattering (SAXS) with a Nanostar U small-angle X-ray scattering system (Bruker, Germany) using Cu Kα radiation ($\lambda = 1.54056$ Å). The crystal structure and phase of products were characterized using wide-angle X-ray diffraction (XRD, Bruker D8, Germany) with Ni-filtered Cu Kα radiation (40 kV, 40 mA). The thermal decomposition behavior of the products was monitored by using a Mettler Toledo TGA/SDTA851 analyzer from 50 to 900 °C in air with a heating rate of 5 °C/min.

Electrochemical characterizations: The electrochemical measurements were conducted by assembling coin-type half cells in an argon-filled glove box. The electrode slurry was prepared by mixing 60 wt. % active material (Si NPs, YS Si@10 mC and YS Si@50 mC), 20 wt. % Super P®, and 20 wt. % carboxymethyl cellulose (CMC) in a planetary mixer (KK-250S). The electrode films were prepared by pasting the slurry on copper foil using a doctor blade to a thickness of 100 μm, which was followed by drying in a vacuum oven at 80 ° C overnight. The working electrodes were prepared by punching the electrode film into discs 0.96 cm in diameter. Lithium foil was employed for both reference and counter electrodes. The electrodes were separated by Celgard separator. The electrolyte was 1.0 M $LiPF_6$ in 3:4:3 (weight ratio) ethylene carbonate (EC) / dimethyl carbonate (DMC) / diethylene carbonate (DEC), with 5 wt. % fluoroethylene carbonate (FEC) additive from Novolyte Technologies. The electrochemical performances were tested by a Land Battery Test System with a cut-off voltage range from 0.005 V to 1.5 V (vs. Li /Li$^+$). Cyclic voltammetry and impedance testing were performed using a Biologic VMP-3 electrochemical workstation from 0.005 V to 1.5 V at a sweep rate of 0.01 mV s^{-1}.

3. Results and discussion

The mesoporous carbon-encapsulated silicon NPs yolk-shell structure can be fabricated through the combination of a sol-gel process and a nanocasting strategy, as schematically shown in Figure 1A. Firstly, the commercial silicon-NPs with the size ranging from ~ 60 to 170 nm (Figure S1A, B) were homogeneously coated with a specially designed sacrificial silica layer *via* the Stöber sol-gel method using tetraethyl orthosilicate (TEOS) as a precursor in an alkaline alcohol/water system, resulting in the formation of the Si@SiO$_2$ core-shell NPs (Figure S1C, D). A thin layer of silicon oxides (SiO$_x$) already exists on the surface of the commercial Si NPs, which promote the deposition of silica through physical interaction (Figure S1B). To identify the crucial internal void space to be created after etching away the sacrificial layer and optimize the performance, the thickness of the middle SiO$_2$ sacrificial layer was specially designed to be 10 and 50 nm by controlling the hydrolysis and condensation of TEOS (Figure 1B, E). Considering the non-uniform size distribution (~ 60-170 nm), and their aggregation, the void space of ~ 10 and 50 nm are rationally designed as insufficient and sufficient protection against the volume expansion of ~ 400 % (The theoretical expansion size are evaluated to be ~ 17.6 and 49.9 nm for 60 and 170 nm Si NPs, respectively). A surfactant-templating sol-gel approach was then used to create a uniform coating of mesoporous silica (*m*SiO$_2$) shells with a thickness of ~ 15 nm by using hexadecyltrimethylammonium bromide (CTAB) as a template (Figure 1C, F and Figure S1E, F) [32, 33]. These resultant Si@SiO$_2$@mSiO$_2$ core-shell NPs have open and worm-like mesopore channels with disordered mesostructures (Figure S2 and S3), which is beneficial for the nanocasting of carbon precursor. This was followed by impregnation of phenolic resin precursor into the mesopore channels through a capillary force and carbonization under nitrogen atmosphere. After selectively leaching out the silica components with the assistance of diluted hydrofluoric acid, the mesoporous carbon-encapsulated Si yolk-shell (YS) structures were obtained and designated as YS Si@*xm*C (where *x* represents the void space). As revealed by the field-emission scanning electron microscope (FE-SEM) images, the silicon NPs are completely sealed inside the hollow mesoporous carbon (*m*C) shells (Figure S4). Transmission electron microscope (TEM) observations of

these YS Si@10*m*C and YS Si@50*m*C NPs clearly show the fascinating yolk-shell structures with an internal void space of ~ 10 and ~ 50 nm, originating from the etched middle silica layer. The outer carbon shells have a uniform thickness that is estimated to be about 15 nm, corresponding well to the mesoporous silica layer. Here, the appropriate thickness of the mesoporous carbon was adopted based on the balance between structural stability of shells and superior silicon ratio. Significantly, the carbon shells present highly porous features, accompanied by open, accessible mesopore channels, and disordered mesostructures (Figure 1D, G and Figure S5).

Nitrogen sorption analysis of both YS Si@10mC and YS Si@50mC NPs show type-IV curves with H2 hysteresis (Figure 2A), demonstrating the presence of mesopores with a uniform size. The pore size distribution peaks strongly center at about 2 nm, measured using the Barrett-Joyner-Halenda (BJH) model (Figure 2B). The Brunauer-Emmett-Teller (BET) surface area and total pore volume are calculated to be as high as 362, 582 m^2g^{-1} and 0.34, 0.51 cm^3g^{-1}, respectively (Table S1). Additionally, the mesoporous carbon coating was also evaluated by X-ray photoelectron spectroscopy (XPS) and Raman spectroscopy. Compared with the bare commercial Si NPs, a manifest C_{1s} peak appears in the XPS survey spectra of YS Si@10*m*C and YS Si@50*m*C; meanwhile, the intensity of Si_{2s} and Si_{2p} dramatically decrease (Figure S6). It implies that the Si NPs are embedded in the mesoporous carbon shells, which is in agreement with the TEM images in large domain (Figure S4B, F). Moreover, a significant decrease is observed in the intensity of the characteristic Si Raman bands around 510 cm^{-1} for the samples YS Si@10*m*C and YS Si@50*m*C, demonstrating the well-sealed structures (Figure 2C). Remarkably, another two broad peaks centered at ~ 1320 and 1590 cm^{-1} are observed, which are assigned to the disorder-induced D band and the graphitic G band, respectively. The strong intensity of D band indicates the amorphous nature of the mesoporous carbon shells. X-ray diffraction (XRD) patterns of the samples YS Si@10*m*C and YS Si@50*m*C display six intense diffraction peaks, similar to commercial silicon NPs with good crystallization. An additional broad peak at about 22.6 ° can be observed, which is typical of amorphous carbon in the yolk-shell structured NPs (Figure 2D). This is

consistent with the Raman results. Furthermore, the mass percentages of silicon in these yolk-shell NPs were determined by thermogravimetric analysis (TGA). The silicon contents are estimated to be 73.4 % and 42.2 % for the samples YS Si@10mC and YS Si@50mC, respectively (Figure S7). Based on the following equation: $Q_{electrode} = w_{Si}*Q_{Si} + w_{mC}*Q_{mC}$, where Q and w refer to the theoretical capacity and the mass ratio of silicon and mesoporous carbon, the theoretical capacities of the samples YS Si@10mC and YS Si@50mC are calculated to be 3139 and 1895 mA h g^{-1}, respectively (Figure S8).

The reasonable design of the yolk-shell structures and the optimized free space are manifested by the electrochemical behavior of the electrodes. All the capacities of cells have been normalized based on the weight of active materials in the form of Si for the pure Si NPs, and yolk-shell Si@mC nanocomposite for the YS Si@10mC and YS Si@50mC. As shown in Figure 3A, the pure commercial Si NPs electrode under-goes a rapid capacity fading, only delivering a reversible capacity of 355 mA h g^{-1} over 50 cycles. The electrochemical performances of the yolk-shell composites are significantly enhanced. After kinetic enhancement at 140 mA g^{-1} for the initial 5 cycles, YS Si@10mC shows initial reversible capacity of 2014 mA h g^{-1}, which accounts for 64.2 % of its theoretical capacity. Its reversible capacity gradually decays to 1440 mA h g^{-1} after 50 cycles. In the following cycles, this electrode suffers from severe structural collapse, leading to steep capacity decay. The capacity retention was only remained at 27.7 % after prolonged cycling to 400 cycles. In contrast, YS Si@50mC presents a high utilization of Si, achieving a reversible capacity of 1272 mA h g^{-1}. Predominant cycling stability is observed, in which the capacity retention is as high as 78.6 % over a long-term 400 cycles. As revealed in the charge and discharge voltage profiles of different cycles (Figure 3B), no obvious capacity decay can be observed in charge profiles at 100th, 200th, 300th, and 400th cycles. Taking advantages of the sufficient free space (~ 50 nm), the designed yolk-shell structure could accommodate the large volume changes in the Si NPs over charge/discharge cycling. As a result, YS Si@50mC is capable of delivering a constant capacity (~ 1000 mA h g^{-1}), even over a long-term 400 cycles. Furthermore, when the current

density increasing from 0.2 to 0.3, 0.6, 1.5, 3, and 6 C (the current density as high as 8.4 A g^{-1}), the YS Si@50mC NPs present decent specific capacities of 1010, 995, 931, 855, 758, and 620 mA h g^{-1}, respectively (Figure 3C). It is notable that the sample YS Si@50mC completely recovers to the initial reversible capacity (~ 1000 mA h g^{-1}) after the heavy-duty cycling, and achieves a stable capacity for the subsequent cycles when the current density recovers to 420 mA g^{-1}, further demonstrating its excellent rate capacity retention behavior and cycling sustainability. In contrast, the sample YS Si@10mC shows dramatic capacity fading, indicating the serious destruction of this electrode's structure (Figure S9). The superior electrochemical performance of YS Si@50mC is also ascribed to its better SEI film (Figure S10), which exhibits much low charge transfer resistance (R_{ct}) and leads to fast diffusion of Li$^+$ ions through the film. Significantly, it is manifest that the sample YS Si@50mC renders superior rate capacity retention, retaining 62.3 % at a high current of 8.4 A g^{-1}, which is favorable compared to other work on Si-anodes reported previously, including hollow Si [16], hollow Si@ppy [34], Si@C sphere [18], Si@C fiber [35], Si@RGO [20], yolk-shell Si@C [22], Si@hydrogel [36], and Si@self-healing-polymer (SHP) [37] (Figure 3D) It is especially noteworthy that YS Si@50mC is far superior to nonporous carbon encapsulated silicon yolk-shell nanoparticles (YS Si@C) on rate performances, which delivered a capacity retention of 91.3 %, 80.7 %, 62.3% and 64 %, 52.9 % , 40.6 % at current density of 2.1, 4.2 and 8.4 A g^{-1}, respectively (Figure 3D). The enhancement of rate capacity retention is believed to be ascribed to the advantageous SEI formed with the aid of mesoporous carbon shells.

The SEM image after 100 cycles displays the structural degradation of YS Si@10mC (Figure 4A). The electrode surface shows obvious cracking; and severe agglomeration of the active materials. In contrast, it can be seen from Figure 4B that the YS Si@50mC electrode features a flat and compact surface in large domain, and it maintains its nano-spherical morphology under the same testing conditions. The YS Si@50mC electrode well maintains its original structure, which proves that the sufficient void space is able to tolerate volume changes of the inner Si, without causing the shell rupture. Scanning transmission electron microscope (STEM) image

and energy-dispersive X-ray (EDX) elemental mapping of YS Si@50mC clearly demonstrate that the yolk-shell nanoparticles are preserved and well-contacted with electrolytes during cycling processes (Figure 4C). These structural variations are in agreement with their electrochemical properties and TEM images of YS Si@10mC and YS Si@50mC electrodes after 100 cycles (Figure S11). Similarly, we can draw the same conclusion from the Coulombic efficiency of the electrodes in Figure 4D. The Coulombic efficiency for the Si NPs fluctuates and is less than 95 %, indicating significant structural changes in the Si NPs. The Coulombic efficiency of the YS Si@10mC is lower than that of YS Si@50mC, and obvious decay appears after 30 cycles, which corresponds to the collapse of the yolk-shell structure and irreversible capacity arising from the formation of updated SEI film. In contrast, the YS Si@50 mC shows stable and high Coulombic efficiency (> 99.1 %) over 100 cycles.

As illustrated in Figure 5A, the buffering space of 10 nm for the sample YS Si@10mC is not enough to accommodate the ~ 400 % volume expansion of Si NPs within the shell. The mesoporous carbon shells could gradually crack and fracture over subsequent cycling, leading to structural collapse of the designed yolk-shell structure. In comparison, the sufficient free space (~ 50 nm) ensures the structure stability and SEI properties of the active materials. The morphology and distribution of SEI of sample YS Si@50mC is characterized at charge state after 3 cycles. A high concentration of lithium layer with the thickness of ~ 20 nm is located at the surface of YS Si@50mC NPs in the electrode, which is corresponding to the SEI film (Figure 5B, C). The Li elemental mapping (Figure 5C) demonstrates that a homogeneous and compact SEI layer is observed along the surface of mesoporous carbon surface instead of the silicon particle. Scanning TEM image of single Si@50mC nanoparticle after 3 cycles and the corresponding Li concentration mapped by electron energy loss spectroscopy (EELS) has shown in Figure 5D and 5E. The EELS spectrum from the outer surface of mesoporous carbon shells shows two typical peaks of the Li K-edge. It corresponds to LiF originating from SEI film (Figure 5F), which results from the decomposition of LiPF$_6$ electrolyte during lithiation [38]. It is obvious that no Li K-edge signal is collected around the lithiated silicon nanoparticle yolk. These results

further prove that the mesoporous carbon shells are not fully accessible to the electrolyte, probably ascribed to the randomness of the mesopores. This elaborate open-ended carbon shells are favorable to the surface infiltration of electrolyte, the favorable SEI film growes due to the anxo-action of mesopores, in which electrolyte is prone to be soaked in and diminutive SEI film is initially formed around the wall of each pore. As a result, a compact SEI layer is produced along the mesoporous carbon shells. Meanwhile, it is well known that the SEI film does not conduct electrons and is almost impenetrable to electrolyte molecules, the electrolyte, therefore, is almost unable to travel through the SEI layer to the Si yolk surface. Combing with the free space design to accommodate the volume expansion of Si, this synergistic effect guarantee the unique yolk-shell Si@mesoporous carbon composites can successfully tackle the two major problems of silicon anode, including the instability of the SEI and the mechanical degradation caused by the large volume changes.

4. Conclusions

In summary, we have rationally designed and successfully fabricated void-containing mesoporous carbon-encapsulated commercial silicon NPs with a yolk-shell structure for stable LIBs. The void space between the Si yolk and the mesoporous carbon shell is reasonably engineered to accommodate the large volume expansion during lithiation and delithiation processes, and optimize the cycling stability. The accessible porosity of the mesoporous carbon shells provides a high electrode-electrolyte contact area, and fast Li^+ penetration. The yolk-shell structured YS Si@50mC mesoporous carbon composites with an enough void space NPs yield long cycle life (~ 1000 mA h g^{-1} after 400 cycles) and excellent rate-capability (62.3 % capacity retained at a high current of 8.4 A g^{-1}). Furthermore, a homogeneous and compact SEI layer is firstly observed on the surface of mesoporous carbon shells, which could be responsible for the superior rate-capability and stability. This work thus offers a promising design for the structure of other anode materials with long cycling performance and good rate capacity retention.

Notes and references

[1] J.M. Tarascon, M. Armand, Nature 414 (2001) 359-367.

[2] K.S. Kang, Y.S. Meng, J. Breger, C.P. Grey, G. Ceder, Science 311 (2006) 977-980.

[3] N.S. Choi, Z.H. Chen, S.A. Freunberger, X.L. Ji, Y.K. Sun, K. Amine, G. Yushin, L.F. Nazar, J. Cho, P.G. Bruce, Angew. Chem. Int. Ed. 51 (2012) 9994-10024.

[4] J.B. Goodenough, K.S. Park, J. Am. Chem. Soc. 135 (2013) 1167-1176.

[5] Y.G. Guo, J.S. Hu, L.J. Wan, Adv. Mater. 20 (2008) 2878-2887.

[6] P.G. Bruce, B. Scrosati, J.M. Tarascon, Angew. Chem. Int. Ed. 47 (2008) 2930-2946.

[7] L.W. Ji, Z. Lin, M. Alcoutlabi, X.W. Zhang, Energy Environ. Sci. 4 (2011) 2682-2699.

[8] R. Teki, M.K. Datta, R. Krishnan, T.C. Parker, T.M. Lu, P.N. Kumta, N. Koratkar, Small 5 (2009) 2236-2242.

[9] H. Wu, Y. Cui, Nano Today 7 (2012) 414-429.

[10] B. Key, M. Morcrette, J.M. Tarascon, C.P. Grey, J. Am. Chem. Soc. 133 (2011) 503-512.

[11] U. Kasavajjula, C.S. Wang, A.J. Appleby, J. Power Sources 163 (2007) 1003-1039.

[12] H. Kim, M. Seo, M.H. Park, J. Cho, Angew. Chem. Int. Ed. 49 (2010) 2146-2149.

[13] M.Y. Ge, J.P. Rong, X. Fang, C.W. Zhou, Nano Lett. 12 (2012) 2318-2323.

[14] W. Wang, P.N. Kumta, ACS Nano 4 (2010) 2233-2241.

[15] M.H. Park, M.G. Kim, J. Joo, K. Kim, J. Kim, S. Ahn, Y. Cui, J. Cho, Nano Lett. 9 (2009) 3844-3847.

[16] X.K. Huang, J. Yang, S. Mao, J.B. Chang, P.B. Hallac, C.R. Fell, B. Metz, J.W. Jiang, P.T. Hurley, J.H. Chen, Adv. Mater. 26 (2014) 4326-4332.

[17] H. Ma, F.Y. Cheng, J. Chen, J.Z. Zhao, C.S. Li, Z.L. Tao, J. Liang, Adv. Mater. 19 (2007) 4067-4070.

[18] W. Li, Y. Tang, W. Kang, Z. Zhang, X. Yang, Y. Zhu, W. Zhang, C.-S. Lee, Small 11(2014) 1345-1351.

[19] X.S. Zhou, Y.X. Yin, L.J. Wan, Y.G. Guo, Adv. Energy Mater. 2 (2012) 1086-1090.

[20] J. Chang, X. Huang, G. Zhou, S. Cui, P.B. Hallac, J. Jiang, P.T. Hurley, J. Chen, Adv. Mater. 26 (2014) 758-764.

[21] L.F. Cui, L.B. Hu, J.W. Choi, Y. Cui, ACS Nano 4 (2010) 3671-3678.

[22] N. Liu, H. Wu, M.T. McDowell, Y. Yao, C.M. Wang, Y. Cui, Nano Lett. 12 (2012) 3315-3321.

[23] S.H. Ng, J.Z. Wang, D. Wexler, K. Konstantinov, Z.P. Guo, H.K. Liu, Angew. Chem. Int. Ed. 45 (2006) 6896-6899.

[24] X.W. Lou, L.A. Archer, Z. Yang, Adv. Mater. 20 (2008) 3987-4019.

[25] J. Liu, S.Z. Qiao, H. Liu, J. Chen, A. Orpe, D. Zhao, G.Q. Lu, Angew. Chem. Int. Ed. 50 (2011) 5947-5951.

[26] G. He, S. Evers, X. Liang, M. Cuisinier, A. Garsuch, L.F. Nazar, ACS Nano 7 (2013) 10920-10930.

[27] J. Wang, W. Li, F. Wang, Y. Xia, A.M. Asiri, D. Zhao, Nanoscale 6 (2014) 3217-3222.

[28] X. Ma, M. Liu, L. Gan, P.K. Tripathi, Y. Zhao, D. Zhu, Z. Xu, L. Chen, Phys. Chem. Chem. Phys. 16 (2014) 4135-4142.

[29] R. Zhang, Y. Du, D. Li, D. Shen, J. Yang, Z. Guo, H.K. Liu, A.A. Elzatahry, D. Zhao, Adv. Mater. 26 (2014) 6749-6755.

[30] L.W. Su, Y. Jing, Z. Zhou, Nanoscale 3 (2011) 3967-3983.

[31] Y. Ren, A.R. Armstrong, F. Jiao, P.G. Bruce, J. Am. Chem. Soc. 132 (2010) 996-1004.

[32] J. Yang, D. Shen, L. Zhou, W. Li, X. Li, C. Yao, R. Wang, A.M. El-Toni, F. Zhang, D. Zhao, Chem. Mater. 25 (2013) 3030-3037.

[33] J. Yang, D. Shen, L. Zhou, W. Li, J. Fan, A.M. El-Toni, W.-x. Zhang, F. Zhang, D. Zhao, Adv. Healthcare Mater. 3 (2014) 1620-1628.

[34] F.H. Du, B. Li, W. Fu, Y.J. Xiong, K.X. Wang, J.S. Chen, Adv. Mater. 26 (2014) 6145-6150.

[35] T.H. Hwang, Y.M. Lee, B.S. Kong, J.S. Seo, J.W. Choi, Nano Lett. 12 (2012) 802-807.

[36] H. Wu, G.H. Yu, L.J. Pan, N.A. Liu, M.T. McDowell, Z.A. Bao, Y. Cui, Nat. Commun. 4 (2013) 6.

[37] C. Wang, H. Wu, Z. Chen, M.T. McDowell, Y. Cui, Z. Bao, Nat. Chem. 5 (2013) 1042-1048.

[38] H. Ryu, T. Kim, K. Kim, J.-H. Ahn, T. Nam, G. Wang, H.-J. Ahn, J. Power Sources 196 (2011) 5186-5190.
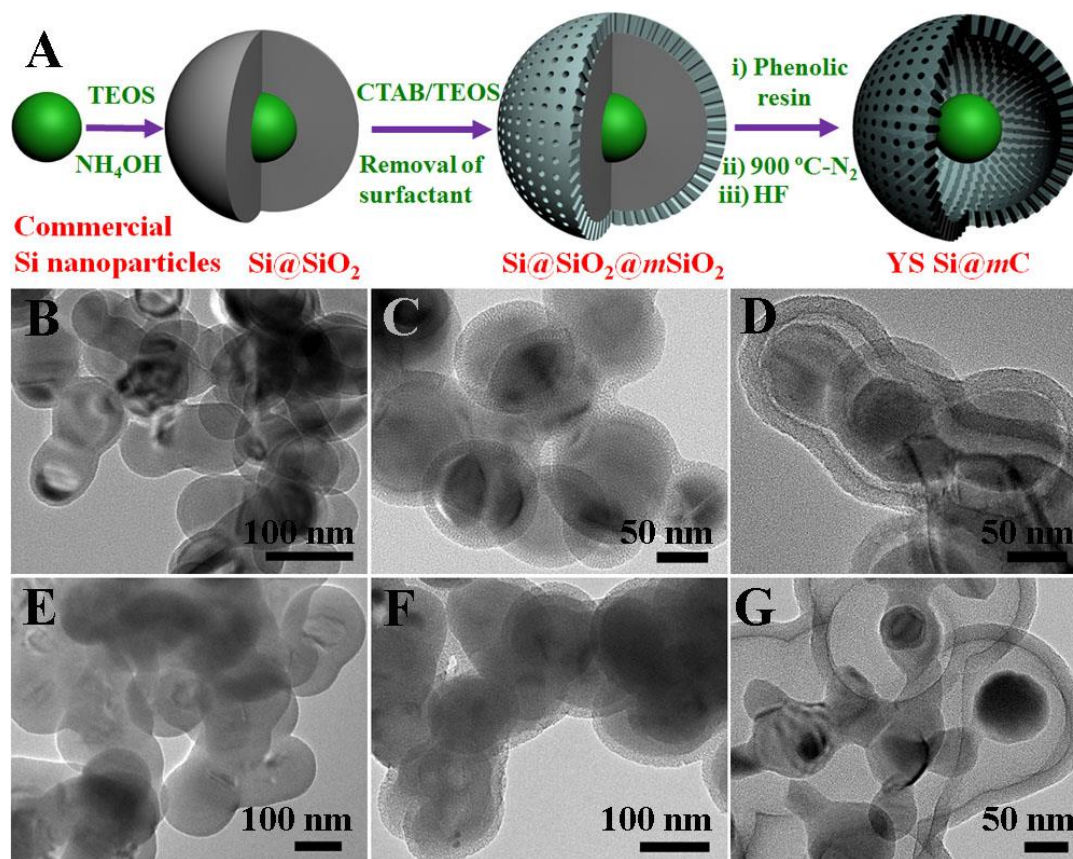
Figure 1 (A) Schematic illustration of the formation process of the mesoporous carbon-encapsulated commercial silicon yolk-shell NPs. (B-G) TEM images of the silica-coated commercial silicon (B) $Si@10SiO_2$ and (E) $Si@50SiO_2$ core-shell NPs with the thickness of 10 and 50 nm, respectively; the mesoporous silica coated (C) $Si@10SiO_2@mSiO_2$ and (F) $Si@50SiO_2@mSiO_2$ core-shell NPs; the mesoporous carbon-encapsulated commercial silicon (D) YS $Si@10mC$ and (G) YS $Si@50mC$ yolk-shell structure with the void space of 10 and 50 nm, respectively.
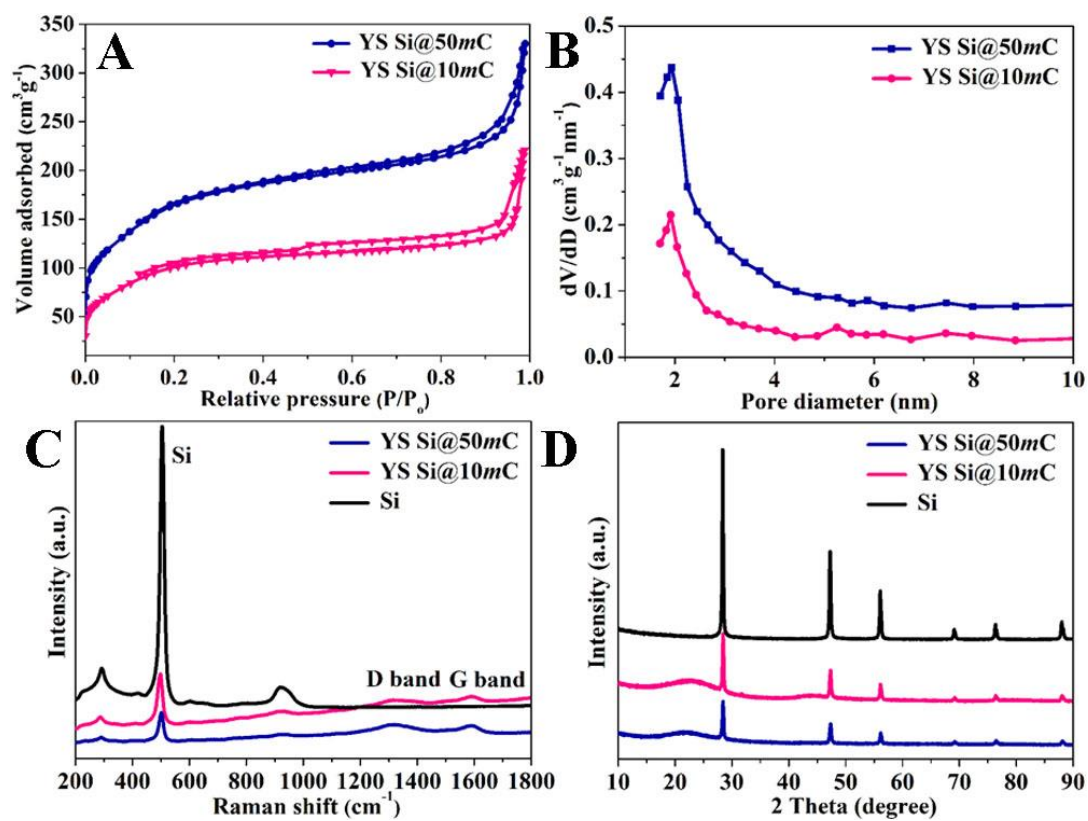
Figure 2 (A) Nitrogen sorption isotherms, (B) pore size distribution curves, (C) Raman spectra, and (D) XRD patterns of the representative samples YS Si@10*m*C and YS Si@50*m*C NPs.
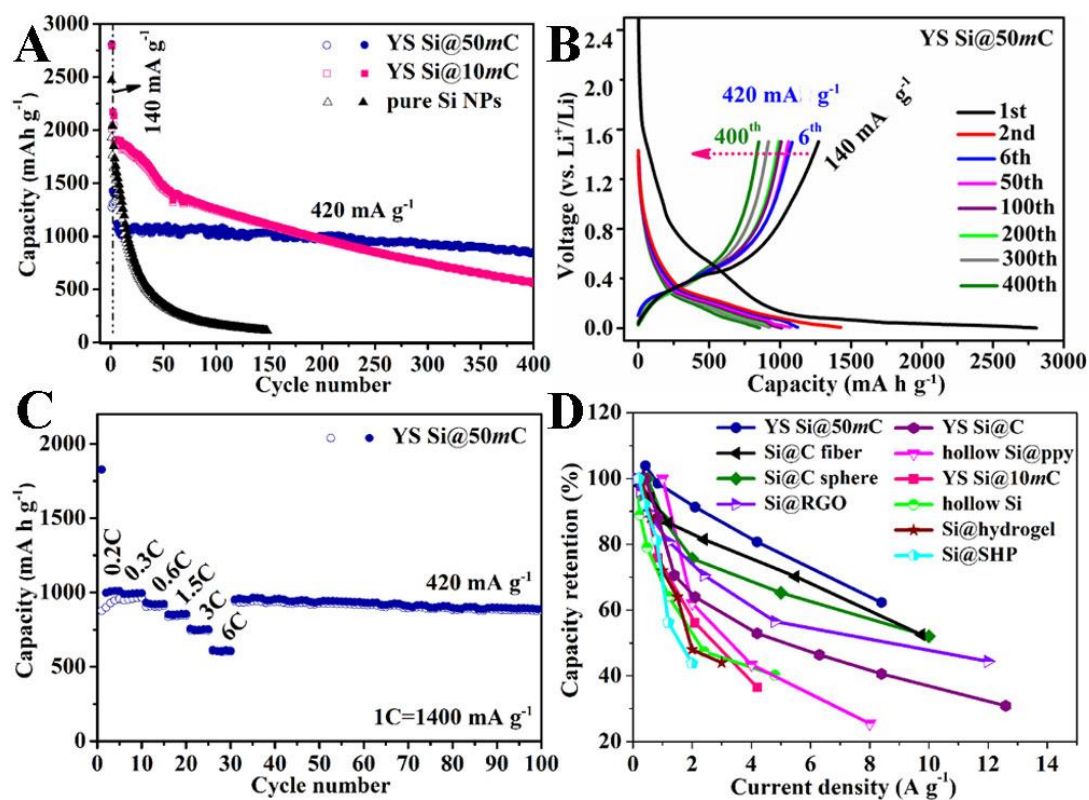
Figure 3 (A) Charge-discharge cycling performance of two represented samples YS Si@50*m*C, YS Si@10*m*C, and commercial Si NPs electrodes. (B) Charge-discharge potential profiles of the samples YS Si@50*m*C at different cycles at a current density of 420 mA g⁻¹. (C) Rate performance of YS Si@50*m*C. (D) Rate capacity retention of YS Si@50*m*C, YS Si@10*m*C, Si@C fiber, Si@C sphere, Si@RGO, YS Si@C, hollow Si@ppy, hollow Si, Si@hydrogel, and Si@SHP electrodes cycled at various current densities.
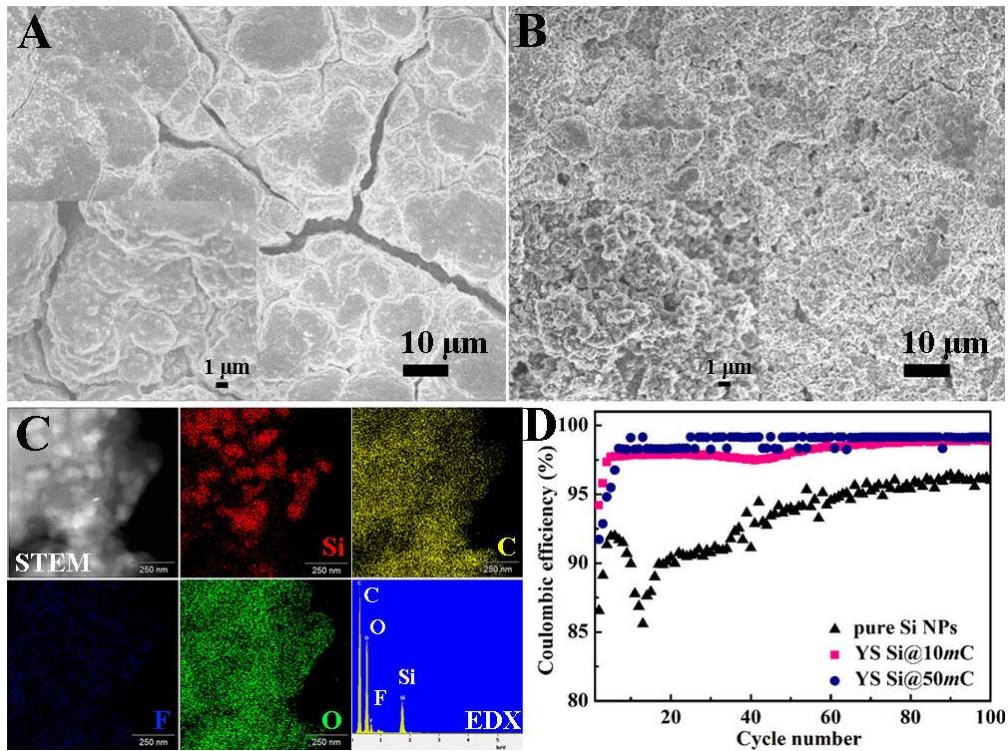
Figure 4 SEM images (A) of YS Si@10*m*C; and (B) YS Si@50*m*C nanoparticle electrodes; (C) scanning transmission electron microscope (STEM), and energy-dispersive X-ray (EDX) elemental mapping of YS Si@50*m*C for Si, C, F, and O, respectively, and EDX spectrum after 100 cycles at a current density of 420 mA g^{-1}. (D) Coulombic efficiency of pure Si NPs, YS Si@10*m*C, and YS Si@50*m*C.
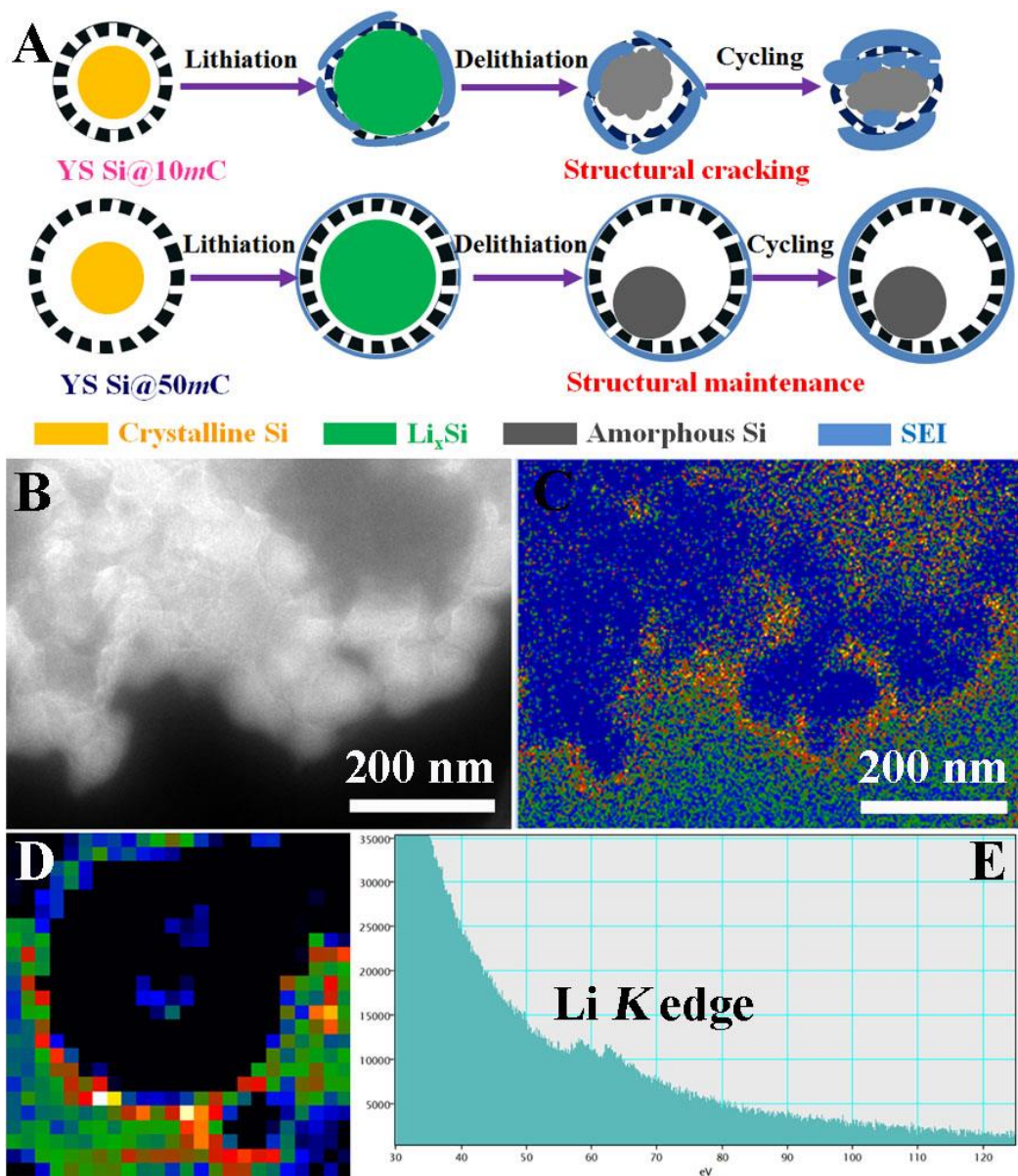
Figure 5 (A) Schematic illustration of lithiation and delithiation processes of YS Si@10*m*C and YS Si@50*m*C electrodes. (B) High-angle annular dark field scanning transmission electron microscope (HAADF-STEM) image (scale bar 200 nm), and (C) Li elemental mapping (yellow dots) (scale bar 200 nm). (D) The scanning TEM (STEM) image of single YS Si@50*m*C nanoparticle at charge state after 3 cycles, the corresponding (E) Li concentration mapped by EELS (blue color corresponding to low concentration of Li *K*-edge, red color corresponding to high concentration of Li *K*-edge); and (F) EELS spectrum of Li *K*-edge from the surface layer.